Journal of Computational Physics 389 (2019) 147–163

Contents lists available at ScienceDirect

Journal of Computational Physics

www.elsevier.com/locate/jcp

Lattice Boltzmann method for general convection-diffusion equations: MRT model and boundary schemes

Mengxin Zhang [a], Weifeng Zhao [a,*], Ping Lin [b,a,**]

[a] Department of Applied Mathematics, University of Science and Technology Beijing, Beijing 100083, China
[b] Division of Mathematics, University of Dundee, Dundee, DD1 4HN, Scotland, United Kingdom

ARTICLE INFO

Article history:
Received 9 September 2018
Received in revised form 27 March 2019
Accepted 28 March 2019
Available online 5 April 2019

Keywords:
Nonlinear convection-diffusion equations
Lattice Boltzmann model
Anti-bounce-back scheme
Single-node boundary schemes
Second-order accuracy

ABSTRACT

This paper is concerned with the lattice Boltzmann method for general convection-diffusion equations. For such equations, we develop a multiple-relaxation-time lattice Boltzmann model and show its consistency under the diffusive scaling. The second-order accuracy of the half-way anti-bounce-back scheme accompanying the present MRT model is justified based on an elegant relation of the collision matrix. Using the half-way anti-bounce-back scheme as a central step, we further construct some parameterized single-node second-order schemes for curved boundaries. The accuracy of the proposed model and boundary schemes are numerically validated with several nonlinear convection-diffusion equations.

1. Introduction

Convection-diffusion equations (CDEs) are widely used to describe the evolution of mass, energy or other physical quantities in industrial processes and natural phenomena, such material sciences [1], fluid mechanics [2] and human health [3]. This class of partial differential equations has been extensively investigated theoretically and numerically (see *e.g.*, [4–7]), and the latter is the focus of this work. Traditional numerical methods for CDEs include finite element, finite volume, finite difference methods, and so on (see *e.g.*, [6–12]). Due to the multidimensionality, nonlinearity and the coupling with other physical fields of CDEs, these methods face difficulties in terms of universality and efficiency [13,14]. In recent years, the lattice Boltzmann method (LBM), which is an efficient approach for hydrodynamics simulations [15,16], has been adapted to CDEs. This method solves the distribution functions instead of the macroscopic variables. Compared with the traditional numerical methods, the LBM is simple in formulation, easy for parallelization and can be extended to high dimensional problems directly [15,16].

There have been various LB models for CDEs or systems coupling CDEs and flow fields in the literature, *e.g.*, [13,14,17–35]. Among them, most models are concerned with linear isotropic or anisotropic CDEs [14,17,18,20,29–35] and those for nonlinear CDEs are relatively few. In [19], a Bhatnagar-Gross-Krook (BGK) model for general nonlinear CDEs is proposed by designing appropriate equilibrium and source term, and it is further extended to the anisotropic case in [23] and modified in [13,21,22]. Though these models are shown to correctly recover the CDEs through the Chapman-Enskog analysis, there are still some limitations in their implementations. First, in the equilibrium of the models, there is an integration related to

* Corresponding author.
** Corresponding author at: Division of Mathematics, University of Dundee, Dundee, DD1 4HN, Scotland, United Kingdom.
E-mail addresses: mxzhang@xs.ustb.edu.cn (M. Zhang), wfzhao@ustb.edu.cn (W. Zhao), plin@maths.dundee.ac.uk (P. Lin).

https://doi.org/10.1016/j.jcp.2019.03.045
0021-9991/

the convection term of the CDE. This integration may not be analytically obtained for some convection terms so that the models can not be used directly (see also [36]). Second, more storage space is needed for discretizing the time derivative in the source terms, which requires special treatments for initializations as well. Another popular model for nonlinear CDEs is the two-relaxation-time (TRT) model [24–28], where assumptions on smallness of the derivatives of convection or diffusion terms have been made to derive the correct macroscopic equations (see Sections 4.3.2 and 5.2 in [24]). However, as pointed out in [19], these assumptions may not be satisfied for some special cases.

Besides the models, the boundary schemes of the LBM for general nonlinear CDEs are not satisfactory. In [23], the non-equilibrium extrapolation scheme for fluid flows [37] is extended to the CDEs and its second-order accuracy is numerically verified, but the scheme involves two lattice nodes and thus does not apply to the case where there are no enough lattice nodes available [38]. Another widely used scheme for CDEs is the anti-bounce-back scheme [25], which is generally first-order accurate except that the boundary is located at the middle of two lattice nodes. Moreover, this scheme is proposed along with the TRT model and its accuracy for general multiple-relaxation-time (MRT) models has not been clearly justified. Based on the anti-bounce-back scheme, second-order schemes for curved boundaries are obtained in [35] by using interpolations between several lattice nodes.

As mentioned above, the existing LB models for general nonlinear CDEs [19,23,21,22,24–28] can not be used for some special CDEs due to the assumptions or the integration term in the models. On the other hand, the boundary schemes in [23,35] involve several lattices nodes and can not be applied when there are no enough nodes available. The latter is of particular importance for simulations of particulate flows with heat transfer [39,40]. In these flows, it is often occurred that two particles are very close so that there is only one computational node between them. In such a case, the aforementioned boundary schemes become invalid.

The aim of this paper is to address the above issues on the model and boundary schemes of the LBM for general nonlinear CDEs. Firstly, we extend the BGK model in [19] to the MRT version and show that the macroscopic equations can be correctly recovered without any assumptions on the macroscopic equations, the integration of convection terms or the time derivative that needs special treatments. The key is the use of the diffusive scaling, which is common for explicit difference schemes of CDEs [6,7]. This scaling is also natural for the LBM since it is indeed a special explicit finite difference scheme. Moreover, we analyze the accuracy of the anti-bounce-back scheme accompanying the present MRT LBM with the Maxwell iteration [43,44]. Based on an elegant relation of the collision matrix of the MRT model found in [45], we justify that the scheme accompanying the MRT model is second-order accurate when the boundary is located at the middle of two lattice nodes (in this case the scheme is usually called half-way anti-bounce-back scheme). To the best of our knowledge, this is the first time that the second-order accuracy of the half-way anti-bounce-back scheme is rigorously analyzed for the MRT model. Furthermore, by using the half-way anti-bounce-back scheme as a central step, we construct some parameterized single-node second-order schemes for curved boundaries with the approach in [45]. Finally, numerical experiments are conducted to validate the proposed model and boundary schemes, and demonstrate the advantages of the MRT model over the BGK model in terms of stability and accuracy.

We would like to point out that the work in [45] focuses on the no-slip boundary conditions of the incompressible Navier-Stokes equations, here we adapt it to the general nonlinear CDEs and find that the relation of the collision matrix and the construction of single-node schemes can be applied directly. However, the analysis in [45] relies on the assumption that the derivative of the fluid density is small as $O(h^2)$, where h is the mesh size, while such assumption is not required in this paper.

The rest of this paper is organized as follows. In Section 2, we provide our MRT LBM for the general CDEs and show its consistency under the diffusive scaling. Section 3 analyzes the accuracy of the anti-bounce-back scheme accompanying the MRT model. Based on the anti-bounce-back scheme, some parameterized single-node second-order schemes are constructed in Section 4. Numerical experiments are conducted in Section 5 to validate the model and boundary schemes. Finally, some conclusions and remarks are given in Section 6. This paper ends with an appendix which provides the derivations of some relations used in Section 2.

2. Lattice Boltzmann model

2.1. Model

Consider a general convection-diffusion equation (CDE)

$$\frac{\partial \phi}{\partial t} + \nabla \cdot \boldsymbol{B}(\phi) = \nabla \cdot [\nu \nabla D(\phi)] + F, \tag{2.1}$$

where $\phi := \phi(\boldsymbol{x}, t)$ is a scalar variable of spatial coordinate $\boldsymbol{x} \in \mathbb{R}^n$ and time t, n is the dimension of space, ∇ is the gradient operator, $\boldsymbol{B}(\phi) := (B_1, B_2, \cdots, B_n)(\phi)$ is a n-vector function of ϕ, $\nu := \nu(\boldsymbol{x}, t)$ is the diffusion coefficient, $D(\phi)$ is a function of ϕ and $F := F(\boldsymbol{x}, t; \phi)$ is the source term. For the CDE (2.1), a multiple-relaxation-time (MRT) LB model reads as

$$f_i(\boldsymbol{x} + \boldsymbol{e}_i\delta_x, t + \delta_t) - f_i(\boldsymbol{x}, t) = -\sum_j (\mathsf{M}^{-1}\mathsf{S}\mathsf{M})_{ij}(f_j - f_j^{(eq)}) + \delta_t \omega_i F, \quad i = 0, 1, 2, \cdots, N-1. \tag{2.2}$$

Here $f_i := f_i(\boldsymbol{x}, t)$ is the i-th distribution function with discrete velocity $\boldsymbol{e}_i$ at position $\boldsymbol{x}$ and time t, δ_x and δ_t are the lattice size and time step, respectively, $\mathsf{M} \in \mathbb{R}^{N\times N}$ is the transformation matrix, $\mathsf{S} = \mathrm{diag}(s_0, s_1, \ldots, s_{N-1})$ is the diagonal relaxation matrix, $f_i^{(eq)}$ is the equilibrium distribution function and ω_i is the i-th weight. To be concrete, we only consider the two dimensional case, *i.e.*, $n = 2$, and use the D2Q9 (two dimensional and nine discrete velocities) lattice with $N = 9$, $\boldsymbol{e}_0 = (0, 0)$, $\boldsymbol{e}_1 = -\boldsymbol{e}_3 = (1, 0)$, $\boldsymbol{e}_2 = -\boldsymbol{e}_4 = (0, 1)$, $\boldsymbol{e}_5 = -\boldsymbol{e}_7 = (1, 1)$ and $\boldsymbol{e}_6 = -\boldsymbol{e}_8 = (-1, 1)$. The transformation matrix M is taken as usual [41,42]:

$$\mathsf{M} = \begin{pmatrix} 1 & 1 & 1 & 1 & 1 & 1 & 1 & 1 & 1 \\ -4 & -1 & -1 & -1 & -1 & 2 & 2 & 2 & 2 \\ 4 & -2 & -2 & -2 & -2 & 1 & 1 & 1 & 1 \\ 0 & 1 & 0 & -1 & 0 & 1 & -1 & -1 & 1 \\ 0 & -2 & 0 & 2 & 0 & 1 & -1 & -1 & 1 \\ 0 & 0 & 1 & 0 & -1 & 1 & 1 & -1 & -1 \\ 0 & 0 & -2 & 0 & 2 & 1 & 1 & -1 & -1 \\ 0 & 1 & -1 & 1 & -1 & 0 & 0 & 0 & 0 \\ 0 & 0 & 0 & 0 & 0 & 1 & -1 & 1 & -1 \end{pmatrix}. \tag{2.3}$$

The key lies in the equilibrium distribution function $f_i^{(eq)}$, which should be carefully designed so that the macroscopic equation can be correctly recovered. Here we employ the equilibrium distribution function proposed in [19] without the integration term, *i.e.*,

$$\begin{aligned} f_i^{(eq)} &= \omega_i[\phi + \frac{\boldsymbol{c}_i \cdot \boldsymbol{B}}{c_s^2} + \frac{(D-\phi)\mathsf{I} : (\boldsymbol{c}_i\boldsymbol{c}_i - c_s^2\mathsf{I})}{2c_s^2}] \\ &= \omega_i[2\phi - D + \frac{3\boldsymbol{e}_i \cdot \boldsymbol{B}}{c} + \frac{3(D-\phi)\boldsymbol{e}_i \cdot \boldsymbol{e}_i}{2}], \end{aligned} \tag{2.4}$$

where the weight coefficients are $\omega_0 = 4/9$, $\omega_{1,2,3,4} = 1/9$ and $\omega_{5,6,7,8} = 1/36$, $\boldsymbol{c}_i = c\boldsymbol{e}_i$, $c = \delta_x/\delta_t$, $c_s = c/\sqrt{3}$, I is the 2×2 unit matrix, and the macroscopic quantity ϕ is defined by the distributions as

$$\phi = \sum_i f_i.$$

It is easy to verify that the above equilibrium distribution satisfies

$$\sum_i f_i^{(eq)} = \phi, \quad \sum_i \boldsymbol{c}_i f_i^{(eq)} = \boldsymbol{B}, \quad \sum_i \boldsymbol{c}_i\boldsymbol{c}_i f_i^{(eq)} = Dc_s^2\mathsf{I}.$$

We show later in the next subsection that the CDE (2.1) can be derived from the LBM (2.2) under the diffusive scaling

$$\delta_x := h, \qquad \delta_t = \eta h^2, \tag{2.5}$$

where η an adjustable parameter. According to the derivation, s_3 and s_5 are determined by the diffusion coefficient ν via

$$s_3 = s_5 = \frac{2}{6\eta\nu + 1}, \tag{2.6}$$

and the other relaxation rates are free. In fact, using diffusive scaling is common for explicit difference schemes of CDEs [6,7], and thus is also natural for the LBM, which is indeed a special explicit finite difference scheme. It will be seen in the following that under the diffusive scaling (2.5), the consistency of the above LBM does not require any assumptions on the macroscopic equations in [24] or the integration and time derivative terms in [19].

2.2. Derivation of the macroscopic equation

In this subsection, we use the Maxwell iteration [43,44] to derive the CDE (2.1) from the LBM (2.2) under the diffusive scaling (2.5). We begin with the Taylor expansion for the left-hand side of (2.2):

$$\mathbf{f}(\boldsymbol{x} + \boldsymbol{e}\delta_x, t + \delta_t) - \mathbf{f}(\boldsymbol{x}, t) \sim \sum_{s=1}^{\infty} h^s D^{(s)}\mathbf{f}(\boldsymbol{x}, t),$$

where

$$\begin{aligned} &\mathbf{f}(\boldsymbol{x} + \boldsymbol{e}\delta_x,\, t + \delta_t) := (f_0(\boldsymbol{x},\, t + \delta_t),\ f_1(\boldsymbol{x} + \boldsymbol{e}_1\delta_x,\, t + \delta_t),\ \ldots,\ f_8(\boldsymbol{x} + \boldsymbol{e}_{q-1}\delta_x,\, t + \delta_t))^T, \\ &\mathbf{f}(\boldsymbol{x},\, t) := (f_0(\boldsymbol{x},\, t),\ f_1(\boldsymbol{x},\, t),\ \ldots,\ f_8(\boldsymbol{x},\, t))^T \end{aligned}$$

and $D^{(s)}$ is the differential operator given by

$$D^{(s)} = \sum_{m+2n=s} \frac{\left(\mathsf{E}_x\partial_x + \mathsf{E}_y\partial_y\right)^m (\eta\partial_t)^n}{m!n!}$$

with m and n two nonnegative integers. Here the matrix $\mathsf{E}_{x/y}$ is defined as

$$\mathsf{E}_{x/y} = \mathrm{diag}(e_{0,x/y}, e_{1,x/y}, \ldots, e_{8,x/y})$$

and $e_{i,x/y}$ denotes the x/y component of $\boldsymbol{e}_i$. Let $\mathbf{f} := \mathbf{f}(\boldsymbol{x}, t)$, $\mathbf{f}^{(eq)} := \mathbf{f}^{(eq)}(\boldsymbol{x}, t)$, $\mathbf{m} = \mathsf{M}\mathbf{f}$, $\mathbf{m}^{(eq)} = \mathsf{M}\mathbf{f}^{(eq)}$ and $\omega = (\omega_0, \omega_1, \cdots, \omega_8)^T$. Then we deduce from (2.2) that

$$\sum_{s=1}^{\infty} h^s D^{(s)}\mathbf{f} = -\mathsf{M}^{-1}\mathsf{S}[\mathbf{m} - \mathbf{m}^{(eq)}] + \eta h^2 \omega F. \tag{2.7}$$

Multiplying the two sides of (2.7) with M, we arrive at

$$\sum_{s=1}^{\infty} h^s \tilde{D}^{(s)}\mathbf{m} = -\mathsf{S}[\mathbf{m} - \mathbf{m}^{(eq)}] + \eta h^2 \mathsf{M}\omega F, \tag{2.8}$$

where

$$\tilde{D}^{(s)} = \sum_{m+2n=s} \frac{\left(\tilde{\mathsf{E}}_x\partial_x + \tilde{\mathsf{E}}_y\partial_y\right)^m (\eta\partial_t)^n}{m!n!}$$

and $\tilde{\mathsf{E}}_{x/y} = \mathsf{M}\mathsf{E}_{x/y}\mathsf{M}^{-1}$. Particularly, we have

$$\tilde{D}^{(1)} = \tilde{\mathsf{E}}_x\partial_x + \tilde{\mathsf{E}}_y\partial_y,$$
$$\tilde{D}^{(2)} = \frac{1}{2}\left(\tilde{\mathsf{E}}_x\partial_x + \tilde{\mathsf{E}}_y\partial_y\right)^2 + \eta\partial_t.$$

The matrices $\tilde{\mathsf{E}}_x$ and $\tilde{\mathsf{E}}_y$ are explicitly given by

$$\tilde{\mathsf{E}}_x := \frac{1}{6}\begin{pmatrix} 0 & 0 & 0 & 6 & 0 & 0 & 0 & 0 & 0 \\ 0 & 0 & 0 & 6 & 6 & 0 & 0 & 0 & 0 \\ 0 & 0 & 0 & 0 & 6 & 0 & 0 & 0 & 0 \\ 4 & 1 & 0 & 0 & 0 & 0 & 0 & 3 & 0 \\ 0 & 2 & 2 & 0 & 0 & 0 & 0 & -6 & 0 \\ 0 & 0 & 0 & 0 & 0 & 0 & 0 & 0 & 6 \\ 0 & 0 & 0 & 0 & 0 & 0 & 0 & 0 & 1 \\ 0 & 0 & 0 & 2 & -2 & 0 & 0 & 0 & 0 \\ 0 & 0 & 0 & 0 & 0 & 4 & 2 & 0 & 0 \end{pmatrix},$$

$$\tilde{\mathsf{E}}_y := \frac{1}{6}\begin{pmatrix} 0 & 0 & 0 & 0 & 0 & 6 & 0 & 0 & 0 \\ 0 & 0 & 0 & 0 & 0 & 6 & 6 & 0 & 0 \\ 0 & 0 & 0 & 0 & 0 & 0 & 6 & 0 & 0 \\ 0 & 0 & 0 & 0 & 0 & 0 & 0 & 0 & 6 \\ 0 & 0 & 0 & 0 & 0 & 0 & 0 & 0 & 6 \\ 4 & 1 & 0 & 0 & 0 & 0 & 0 & -3 & 0 \\ 0 & 2 & 2 & 0 & 0 & 0 & 0 & 6 & 0 \\ 0 & 0 & 0 & 0 & 0 & -2 & 2 & 0 & 0 \\ 0 & 0 & 0 & 4 & 2 & 0 & 0 & 0 & 0 \end{pmatrix}.$$

For simplicity, we assume that all the relaxation rates are positive, *i.e.*, $s_i > 0$ for $0 \le i \le 8$, such that S is invertible (singular S can be handled in exactly the same way as in [43]). Then we denote

$$\mathsf{L} = \sum_{s=1}^{\infty} h^s \tilde{D}^{(s)}$$

and rewrite Eq. (2.8) as

$$\mathbf{m} = \mathbf{m}^{(eq)} - \mathsf{S}^{-1}\mathsf{L}\mathbf{m} + \eta h^2 \mathsf{S}^{-1}\mathsf{M}\omega F. \tag{2.9}$$

Using the Maxwell iteration [43,44] for the above equation, *i.e.*, substituting (2.9) into its right hand side, we obtain

$$\mathbf{m} = \mathbf{m}^{(eq)} - \mathsf{S}^{-1}\mathsf{L}\mathbf{m}^{(eq)} + O(h^2).$$

Similarly, iterating (2.9) twice, we arrive at

$$\begin{aligned}\mathbf{m} = \mathbf{m}^{(eq)} &- \mathsf{S}^{-1}\mathsf{L}\mathbf{m}^{(eq)} + \mathsf{S}^{-1}\mathsf{L}\mathsf{S}^{-1}\mathsf{L}\mathbf{m}^{(eq)} + \eta h^2\mathsf{S}^{-1}\mathsf{M}\omega F \\ &- \mathsf{S}^{-1}\mathsf{L}\mathsf{S}^{-1}\mathsf{L}\mathsf{S}^{-1}\mathsf{L}\mathbf{m}^{(eq)} - \eta h^2\mathsf{S}^{-1}\mathsf{L}\mathsf{S}^{-1}\mathsf{M}\omega F + O(h^4).\end{aligned}$$

This can be simplified by the definitions of L and $\tilde{D}^{(s)}$ as

$$\begin{aligned}\mathbf{m} = \mathbf{m}^{(eq)} &- \mathsf{S}^{-1}[h\tilde{D}^{(1)} + h^2\tilde{D}^{(2)} + h^3\tilde{D}^{(3)}]\mathbf{m}^{(eq)} \\ &+ [h\mathsf{S}^{-1}\tilde{D}^{(1)} + h^2\mathsf{S}^{-1}\tilde{D}^{(2)}]^2\mathbf{m}^{(eq)} + \eta h^2\mathsf{S}^{-1}\mathsf{M}\omega F \\ &- h^3[\mathsf{S}^{-1}\tilde{D}^{(1)}]^3\mathbf{m}^{(eq)} - \eta h^3\mathsf{S}^{-1}\tilde{D}^{(1)}\mathsf{S}^{-1}\mathsf{M}\omega F + O(h^4).\end{aligned} \tag{2.10}$$

Now we use (2.10) to derive the macroscopic equation. To this end, we denote $\boldsymbol{B} = (B_1, B_2)$ and explicitly give

$$\mathbf{m}^{(eq)} = \begin{pmatrix} \phi \\ 2D - 4\phi \\ 3\phi - 2D \\ \eta h B_1 \\ -\eta h B_1 \\ \eta h B_2 \\ -\eta h B_2 \\ 0 \\ 0 \end{pmatrix} \tag{2.11}$$

and

$$\tilde{D}^{(1)}\mathbf{m}^{(eq)} = \tilde{\mathsf{E}}_x\partial_x\mathbf{m}^{(eq)} + \tilde{\mathsf{E}}_y\partial_y\mathbf{m}^{(eq)} = \partial_x\begin{pmatrix} \eta h B_1 \\ 0 \\ -\eta h B_1 \\ \frac{1}{3}D \\ -\frac{1}{3}\phi \\ 0 \\ 0 \\ \frac{2}{3}\eta h B_1 \\ \frac{1}{3}\eta h B_2 \end{pmatrix} + \partial_y\begin{pmatrix} \eta h B_2 \\ 0 \\ -\eta h B_2 \\ 0 \\ 0 \\ \frac{1}{3}D \\ -\frac{1}{3}\phi \\ -\frac{2}{3}\eta h B_2 \\ \frac{1}{3}\eta h B_1 \end{pmatrix}. \tag{2.12}$$

From this we see that the 0-th component of $\tilde{D}^{(1)}\mathbf{m}^{(eq)}$ is

$$[\tilde{D}^{(1)}\mathbf{m}^{(eq)}]_0 = \eta h \nabla \cdot \boldsymbol{B}. \tag{2.13}$$

Moreover, we show in Appendix that

$$[\tilde{D}^{(3)}\mathbf{m}^{(eq)}]_0 = O(h), \tag{2.14a}$$

$$\{[\mathsf{S}^{-1}\tilde{D}^{(1)}]^3\mathbf{m}^{(eq)}\}_0 = O(h), \tag{2.14b}$$

$$[\tilde{D}^{(1)}\mathsf{S}^{-1}\tilde{D}^{(2)}\mathbf{m}^{(eq)}]_0 = O(h), \tag{2.14c}$$

$$[\tilde{D}^{(2)}\mathsf{S}^{-1}\tilde{D}^{(1)}\mathbf{m}^{(eq)}]_0 = O(h). \tag{2.14d}$$

Using these relations, (2.13) and the definition $\phi = \sum_i f_i$, we obtain the 0-th component of (2.10):

$$\begin{aligned}\phi = \phi &- s_0\eta h^2\nabla\cdot\boldsymbol{B} - s_0h^2[\tilde{D}^{(2)}\mathbf{m}^{(eq)}]_0 \\ &+ h^2\{[\mathsf{S}^{-1}\tilde{D}^{(1)}]^2\mathbf{m}^{(eq)}\}_0 + \eta h^2 s_0 F + O(h^4),\end{aligned} \tag{2.15}$$

which can be further written as

$$\begin{aligned}s_0\eta h^2\nabla\cdot\boldsymbol{B} - \eta h^2 s_0 F &= -s_0h^2[\tilde{D}^{(2)}\mathbf{m}^{(eq)}]_0 + h^2\{[\mathsf{S}^{-1}\tilde{D}^{(1)}]^2\mathbf{m}^{(eq)}\}_0 + O(h^4) \\ &= -s_0h^2\partial_t\phi - s_0h^2[\tilde{D}^{(1)}(\frac{1}{2}\mathsf{I} - \mathsf{S}^{-1})\tilde{D}^{(1)}\mathbf{m}^{(eq)}]_0 + O(h^4).\end{aligned} \tag{2.16}$$

Next we compute $[\tilde{D}^{(1)}(\frac{1}{2}\mathsf{I}-\mathsf{S}^{-1})\tilde{D}^{(1)}]_0$. It is direct to see that the first row of the matrix $\tilde{D}^{(1)}(\frac{1}{2}\mathsf{I}-\mathsf{S}^{-1})$ is

$$(0,0,0,(\frac{1}{2}-\frac{1}{s_3})\partial_x,0,(\frac{1}{2}-\frac{1}{s_5})\partial_y,0,0,0). \tag{2.17}$$

This and (2.12) yield

$$[\tilde{D}^{(1)}(\frac{1}{2}\mathsf{I}-\mathsf{S}^{-1})\tilde{D}^{(1)}]_0=\partial_x[\frac{1}{3}(\frac{1}{2}-\frac{1}{s_3})\partial_x D]+\partial_y[\frac{1}{3}(\frac{1}{2}-\frac{1}{s_5})\partial_y D].$$

Substituting the above expression into (2.16), we obtain the CDE

$$\frac{\partial\phi}{\partial t}+\nabla\cdot\boldsymbol{B}=\nabla\cdot(\nu\nabla D)+F+O(h^2), \tag{2.18}$$

where $\nu=\frac{1}{3\eta}(\frac{1}{s_3}-\frac{1}{2})$ and $s_3=s_5$. Note that the error in (2.18) is $O(h^2)$, thus the MRT LBM (2.2) together with the equilibrium distribution function (2.4) is second-order accurate.

3. Accuracy of the anti-bounce-back scheme

We further consider boundary treatments of the MRT LBM (2.2) for the Dirichlet boundary condition

$$\phi(\boldsymbol{x},t)=\psi(\boldsymbol{x},t),\quad \boldsymbol{x}\in\partial\Omega, \tag{3.19}$$

where $\psi(\boldsymbol{x},t)$ is a given function of the boundary point $\boldsymbol{x}$ and time t, and $\partial\Omega$ is the boundary. For this boundary condition, a widely used scheme is the anti-bounce-back scheme proposed in [25] along with the TRT model. Here we justify its accuracy for the MRT model (2.2) with the expansion obtained by the Maxwell iteration in the previous subsection.

Instead of analyzing the anti-bounce-back scheme directly, we concentrate on a scheme of the following general form

$$f_i(\boldsymbol{x}_f,t+\delta_t)=-f'_{\bar{i}}(\boldsymbol{x}_f,t)+G, \tag{3.20}$$

where $\boldsymbol{x}_f$ is the internal lattice node near the boundary point $\boldsymbol{x}_b$ (see Fig. 1 below), $\bar{i}$ is defined such that $\boldsymbol{e}_{\bar{i}}=-\boldsymbol{e}_i$, $f'_{\bar{i}}:=f'_{\bar{i}}(\boldsymbol{x}_f,t)$ is the post-collision distribution

$$f'_{\bar{i}}=f_{\bar{i}}-\sum_j(\mathsf{M}^{-1}\mathsf{S}\mathsf{M})_{\bar{i}j}(f_j-f_j^{(eq)})+\delta_t\omega_{\bar{i}}F,$$

and G is to be determined for the consistency with the boundary condition (3.19).

Denote

$$\mathsf{A}=\mathsf{M}^{-1}\mathsf{S}\mathsf{M} \tag{3.21}$$

and recall that A is invertible due to the invertibility of S (again, singular S can be handled as in [43]). Then it follows from (2.10) that

$$f_i=f_i^{(eq)}+h\sum_j(\mathsf{A}^{-1})_{ij}(e_j\cdot\nabla)f_j^{(eq)}+O(h^2). \tag{3.22}$$

Note that the diffusive scaling (2.5) means

$$c=\frac{\delta_x}{\delta_t}=\frac{1}{\eta h}$$

and thus the equilibrium (2.4) can be rewritten as

$$f_i^{(eq)}=\omega_i[2\phi-D+3\eta h\boldsymbol{e}_i\cdot\boldsymbol{B}+\frac{3}{2}\boldsymbol{e}_i\cdot\boldsymbol{e}_i(D-\phi)]. \tag{3.23}$$

Substituting this into (3.22) gives

$$f_i=f_i^{(eq)}+h\sum_j(\mathsf{A}^{-1})_{ij}\omega_j(\boldsymbol{e}_j\cdot\nabla)[(2\phi-D)+\frac{3}{2}\boldsymbol{e}_j\cdot\boldsymbol{e}_j(D-\phi)]+O(h^2). \tag{3.24}$$

Having the expansion (3.24), we expand each term in (3.20) at the boundary point $\boldsymbol{x}_b$, the intersection of the grid line and the boundary (See Fig. 1). To this end, we refer to Fig. 1 and denote

$$\boldsymbol{x}_f=\boldsymbol{x}_b+\gamma h\boldsymbol{e}_i.$$

Using this, (3.23) and (3.24), we expand $f_i(\boldsymbol{x}_f, t+\delta_t)$ at $\boldsymbol{x}_b$ as

$$\begin{aligned} f_i(\boldsymbol{x}_f, t+\delta_t) &= f_i(\boldsymbol{x}_b + \gamma h\boldsymbol{e}_i, t+\eta h^2) \\ &= f_i(\boldsymbol{x}_b, t) + \gamma h\boldsymbol{e}_i\cdot\nabla f_i(\boldsymbol{x}_b, t) + O(h^2) \\ &= f_i^{(eq)}(\boldsymbol{x}_b, t) + h\sum_j (\mathsf{A}^{-1})_{ij}\omega_j(\boldsymbol{e}_j\cdot\nabla)[(2\phi - D) + \frac{3}{2}\boldsymbol{e}_j\cdot\boldsymbol{e}_j(D-\phi)](\boldsymbol{x}_b, t) \\ &\quad + \gamma h\omega_i(\boldsymbol{e}_i\cdot\nabla)[(2\phi - D) + \frac{3}{2}\boldsymbol{e}_i\cdot\boldsymbol{e}_i(D-\phi)](\boldsymbol{x}_b, t) + O(h^2). \end{aligned} \tag{3.25}$$

Similarly, $f_{\bar{i}}'(\boldsymbol{x}_f, t)$ can be expanded as

$$\begin{aligned} f_{\bar{i}}'(\boldsymbol{x}_f, t) &= f_{\bar{i}}(\boldsymbol{x}_f - h\boldsymbol{e}_i, t+\delta_t) = f_{\bar{i}}(\boldsymbol{x}_b - (1-\gamma)h\boldsymbol{e}_i, t+\eta h^2) \\ &= f_{\bar{i}}(\boldsymbol{x}_b, t) - (1-\gamma)h\boldsymbol{e}_i\cdot\nabla f_{\bar{i}}(\boldsymbol{x}_b, t) + O(h^2) \\ &= f_{\bar{i}}^{(eq)}(\boldsymbol{x}_b, t) + h\sum_j (\mathsf{A}^{-1})_{\bar{i}j}\omega_j(\boldsymbol{e}_j\cdot\nabla)[(2\phi - D) + \frac{3}{2}\boldsymbol{e}_j\cdot\boldsymbol{e}_j(D-\phi)](\boldsymbol{x}_b, t) \\ &\quad - (1-\gamma)h\omega_{\bar{i}}(\boldsymbol{e}_i\cdot\nabla)[(2\phi - D) + \frac{3}{2}\boldsymbol{e}_{\bar{i}}\cdot\boldsymbol{e}_{\bar{i}}(D-\phi)](\boldsymbol{x}_b, t) + O(h^2) \\ &= f_{\bar{i}}^{(eq)}(\boldsymbol{x}_b, t) + h\sum_j (\mathsf{A}^{-1})_{\bar{i}j}\omega_j(\boldsymbol{e}_j\cdot\nabla)[(2\phi - D) + \frac{3}{2}\boldsymbol{e}_j\cdot\boldsymbol{e}_j(D-\phi)](\boldsymbol{x}_b, t) \\ &\quad - (1-\gamma)h\omega_i(\boldsymbol{e}_i\cdot\nabla)[(2\phi - D) + \frac{3}{2}\boldsymbol{e}_i\cdot\boldsymbol{e}_i(D-\phi)](\boldsymbol{x}_b, t) + O(h^2). \end{aligned} \tag{3.26}$$

With expansions (3.25) and (3.26), we have

$$\begin{aligned} R_i &:= f_i(\boldsymbol{x}_f, t+\delta_t) + f_{\bar{i}}'(\boldsymbol{x}_f, t) - G \\ &= f_i^{(eq)}(\boldsymbol{x}_b, t) + f_{\bar{i}}^{(eq)}(\boldsymbol{x}_b, t) + h\sum_j [(\mathsf{A}^{-1})_{ij} + (\mathsf{A}^{-1})_{\bar{i}j}]\omega_j(\boldsymbol{e}_j\cdot\nabla)[(2\phi - D) + \frac{3}{2}\boldsymbol{e}_j\cdot\boldsymbol{e}_j(D-\phi)](\boldsymbol{x}_b, t) \\ &\quad + (2\gamma - 1)h\omega_i(\boldsymbol{e}_i\cdot\nabla)[(2\phi - D) + \frac{3}{2}\boldsymbol{e}_i\cdot\boldsymbol{e}_i(D-\phi)](\boldsymbol{x}_b, t) - G + O(h^2) \\ &= \omega_i[4\phi - 2D + 3\boldsymbol{e}_i\cdot\boldsymbol{e}_i(D-\phi)](\boldsymbol{x}_b, t) - G \\ &\quad + h\sum_j [(\mathsf{A}^{-1})_{ij} + (\mathsf{A}^{-1})_{\bar{i}j}]\omega_j(\boldsymbol{e}_j\cdot\nabla)[(2\phi - D) + \frac{3}{2}\boldsymbol{e}_j\cdot\boldsymbol{e}_j(D-\phi)](\boldsymbol{x}_b, t) \\ &\quad + (2\gamma - 1)h\omega_i(\boldsymbol{e}_i\cdot\nabla)[(2\phi - D) + \frac{3}{2}\boldsymbol{e}_i\cdot\boldsymbol{e}_i(D-\phi)](\boldsymbol{x}_b, t) + O(h^2). \end{aligned} \tag{3.27}$$

To eliminate the zeroth-order term in the above equation, it is required that

$$G = \omega_i[4\phi - 2D + 3\boldsymbol{e}_i\cdot\boldsymbol{e}_i(D-\phi)](\boldsymbol{x}_b, t).$$

This and the boundary condition (3.19) yield the expression of G:

$$G = \omega_i[4\psi - 2D(\psi) + 3\boldsymbol{e}_i\cdot\boldsymbol{e}_i(D(\psi) - \psi)](\boldsymbol{x}_b, t). \tag{3.28}$$

Thus we obtain the boundary scheme

$$f_i(\boldsymbol{x}_f, t+\delta_t) = -f_{\bar{i}}'(\boldsymbol{x}_f, t) + \omega_i[4\psi - 2D(\psi) + 3\boldsymbol{e}_i\cdot\boldsymbol{e}_i(D(\psi) - \psi)](\boldsymbol{x}_b, t), \tag{3.29}$$

which degenerates to the widely used one for linear CDEs when $D \equiv \phi$ (see *e.g.*, [29]).

Moreover, we show how the first-order term in (3.27) can be eliminated. We recall from [45] that the matrix A defined in (3.21) with the transformation matrix (2.3) satisfies

$$(\mathsf{A}^{-1})_{ij} = (\mathsf{A}^{-1})_{\bar{i}\bar{j}} \tag{3.30}$$

($\mathsf{A}_{ij} = \mathsf{A}_{\bar{i}\bar{j}}$ also holds true). Based on this relation, we have

Proposition 3.1. *If the matrix* A *satisfies* (3.30)*, then it holds that*

$$\sum_j [(\mathsf{A}^{-1})_{ij} + (\mathsf{A}^{-1})_{\bar{i}j}]\omega_j(\boldsymbol{e}_j\cdot\nabla)[(2\phi - D) + \frac{3}{2}\boldsymbol{e}_j\cdot\boldsymbol{e}_j(D-\phi)] = 0. \tag{3.31}$$

Proof. Using (3.30), we directly compute

$$\begin{aligned}
&\sum_j (\mathsf{A}^{-1})_{\bar{i}j}\omega_j(\boldsymbol{e}_j\cdot\nabla)[(2\phi - D) + \frac{3}{2}\boldsymbol{e}_j\cdot\boldsymbol{e}_j(D-\phi)]\\
&= \sum_j (\mathsf{A}^{-1})_{\bar{i}\bar{j}}\omega_{\bar{j}}(\boldsymbol{e}_{\bar{j}}\cdot\nabla)[(2\phi - D) + \frac{3}{2}\boldsymbol{e}_{\bar{j}}\cdot\boldsymbol{e}_{\bar{j}}(D-\phi)]\\
&= \sum_j (\mathsf{A}^{-1})_{ij}\omega_{\bar{j}}(\boldsymbol{e}_{\bar{j}}\cdot\nabla)[(2\phi - D) + \frac{3}{2}\boldsymbol{e}_{\bar{j}}\cdot\boldsymbol{e}_{\bar{j}}(D-\phi)]\\
&= -\sum_j (\mathsf{A}^{-1})_{ij}\omega_j(\boldsymbol{e}_j\cdot\nabla)[(2\phi - D) + \frac{3}{2}\boldsymbol{e}_j\cdot\boldsymbol{e}_j(D-\phi)],
\end{aligned} \tag{3.32}$$

and (3.31) immediately follows. □

With (3.31) and the expression of G in (3.28), the error (3.27) can be simplified as

$$R_i = (2\gamma - 1)h\omega_i(\boldsymbol{e}_i\cdot\nabla)[(2\phi - D) + \frac{3}{2}\boldsymbol{e}_i\cdot\boldsymbol{e}_i(D-\phi)](\boldsymbol{x}_b, t) + O(h^2). \tag{3.33}$$

If and only if $\gamma = \frac{1}{2}$, the first-order term of R_i is eliminated, *i.e.*, $R_i = O(h^2)$. This indicates that the scheme (3.29) has second-order accuracy when $\gamma = \frac{1}{2}$, and is first-order accurate otherwise.

Actually, Scheme (3.29) is exactly the anti-bounce-back scheme of the following form [25]

$$f_i(\boldsymbol{x}_f, t+\delta_t) = -f_{\bar{i}}'(\boldsymbol{x}_f, t) + 2f_i^{(eq),+}(\boldsymbol{x}_b, t),$$

where $f_i^{(eq),+} = \omega_i[2\phi - D + \frac{3(D-\phi)\boldsymbol{e}_i\cdot\boldsymbol{e}_i}{2}]$ is the even part of $f_i^{(eq)}$ in (2.4). In particular, when $\gamma = \frac{1}{2}$, *i.e.*, the boundary is located at the middle of two lattice nodes, the scheme is usually called the half-way anti-bounce-back scheme. In [25], the above scheme is proposed along with the TRT model. Moreover, its second-order accuracy relies on the assumption $\nabla J = O(\epsilon^2)$, where $J = \boldsymbol{c}\cdot\overrightarrow{f}$, $\boldsymbol{c}$ is a certain discrete velocity, $\overrightarrow{f}$ is the convection term of the CDE and ϵ is a small expansion parameter without a clear definition (see Page 1203 of [25]). Here we clearly justify the accuracy of the anti-bounce-back scheme for the MRT model, and the justification does not need any assumptions but crucially relies on the relation (3.30), which is an identity for the MRT model.

Remark 3.2. The derivation and analysis above can be straightforwardly adapted to the bounce-back scheme for the Neumann boundary conditions of the CDEs. We have done this and find that the relation (3.30) is also crucial for its second-order accuracy.

4. Single-node schemes

In this section, we base on the half-way anti-bounce-back scheme (3.29) to construct a family of single-node second-order boundary schemes with the approach in [45]. The construction in [45] focuses on the no-slip boundary conditions of the incompressible Navier-Stokes equations, here we extend it to the Dirichlet boundary condition of the general nonlinear CDE (2.1).

To begin with, we refer to Fig. 1 and denote by $\boldsymbol{x}_b, \boldsymbol{x}_l$ and $\boldsymbol{x}_r$ the intersection of the given boundary and the grid line in the $\boldsymbol{e}_i$-direction, and the left and right neighboring lattice nodes of $\boldsymbol{x}_f$. Namely,

$$\begin{aligned}
&\boldsymbol{x}_l = \boldsymbol{x}_f + h\boldsymbol{e}_i, \qquad \boldsymbol{x}_r = \boldsymbol{x}_f - h\boldsymbol{e}_i,\\
&\boldsymbol{x}_b = \boldsymbol{x}_f - \gamma h\boldsymbol{e}_i, \qquad \gamma \in (0, 1].
\end{aligned}$$

Additionally, let l be a non-negative number and take (see Fig. 1)

$$\boldsymbol{x}_1 = \boldsymbol{x}_f - lh\boldsymbol{e}_i, \qquad \boldsymbol{x}_2 = 2\boldsymbol{x}_b - \boldsymbol{x}_1.$$

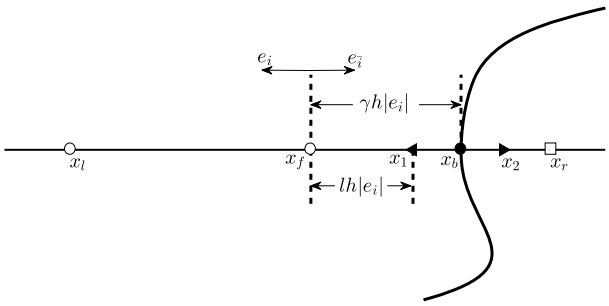

Fig. 1. The thin solid straight line is the grid line and the thick curved line is the boundary. White circles (○) are the lattice nodes in the computational domain, the black circle (●) is the intersection of the boundary and the grid line, and the square box (□) is out of the computational domain.

With $\boldsymbol{x}_1$ and $\boldsymbol{x}_2$ defined above, we firstly interpolate the distribution function $f_i(\boldsymbol{x}_f, t+\delta_t)$ with those at $\boldsymbol{x}_l$ and $\boldsymbol{x}_1$ by

$$f_i(\boldsymbol{x}_f, t+\delta_t) = \frac{l}{1+l} f_i(\boldsymbol{x}_l, t+\delta_t) + \frac{1}{1+l} f_i(\boldsymbol{x}_1, t+\delta_t).$$

Notice that $l \geq 0$. Thanks to the advection $f_i(\boldsymbol{x}_l, t+\delta_t) = f_i'(\boldsymbol{x}_f, t)$, the above equation can be rewritten as

$$f_i(\boldsymbol{x}_f, t+\delta_t) = \frac{l}{1+l} f_i'(\boldsymbol{x}_f, t) + \frac{1}{1+l} f_i(\boldsymbol{x}_1, t+\delta_t). \tag{4.34}$$

Since the boundary point $\boldsymbol{x}_b$ is located at the middle of $\boldsymbol{x}_1$ and $\boldsymbol{x}_2$, we compute $f_i(\boldsymbol{x}_1, t+\delta_t)$ in (4.34) with the half-way anti-bounce-back scheme (see (3.29))

$$f_i(\boldsymbol{x}_1, t+\delta_t) = -f_{\bar{i}}(\boldsymbol{x}_2, t+\delta_t) + \omega_i[4\psi - 2D(\psi) + 3\boldsymbol{e}_i \cdot \boldsymbol{e}_i(D(\psi) - \psi)](\boldsymbol{x}_b, t). \tag{4.35}$$

It remains to compute $f_{\bar{i}}(\boldsymbol{x}_2, t+\delta_t)$ in (4.35). We interpolate it with the distribution functions at $\boldsymbol{x}_f$ and $\boldsymbol{x}_r$:

$$f_{\bar{i}}(\boldsymbol{x}_2, t+\delta_t) = (1+l-2\gamma) f_{\bar{i}}(\boldsymbol{x}_f, t+\delta_t) + (2\gamma - l) f_{\bar{i}}(\boldsymbol{x}_r, t+\delta_t).$$

Again, using the advection $f_{\bar{i}}(\boldsymbol{x}_r, t+\delta_t) = f_{\bar{i}}'(\boldsymbol{x}_f, t)$, we obtain

$$f_{\bar{i}}(\boldsymbol{x}_2, t+\delta_t) = (1+l-2\gamma) f_{\bar{i}}(\boldsymbol{x}_f, t+\delta_t) + (2\gamma - l) f_{\bar{i}}'(\boldsymbol{x}_f, t). \tag{4.36}$$

Combining Eqs. (4.34)–(4.36) gives

$$\begin{aligned} f_i(\boldsymbol{x}_f, t+\delta_t) = &-\frac{1+l-2\gamma}{1+l} f_{\bar{i}}(\boldsymbol{x}_f, t+\delta_t) + \frac{l}{1+l} f_i'(\boldsymbol{x}_f, t) \\ &- \frac{2\gamma - l}{1+l} f_{\bar{i}}'(\boldsymbol{x}_f, t) + \frac{1}{1+l}\omega_i[4\psi - 2D(\psi) + 3\boldsymbol{e}_i \cdot \boldsymbol{e}_i(D(\psi) - \psi)](\boldsymbol{x}_b, t). \end{aligned} \tag{4.37}$$

Furthermore, with the approximation

$$f_{\bar{i}}(\boldsymbol{x}_f, t+\delta_t) \approx f_{\bar{i}}(\boldsymbol{x}_f, t) \tag{4.38}$$

in Eq. (4.37), we arrive at the following single-node scheme

$$\begin{aligned} f_i(\boldsymbol{x}_f, t+\delta_t) = &-\frac{1+l-2\gamma}{1+l} f_{\bar{i}}(\boldsymbol{x}_f, t) + \frac{l}{1+l} f_i'(\boldsymbol{x}_f, t) \\ &- \frac{2\gamma - l}{1+l} f_{\bar{i}}'(\boldsymbol{x}_f, t) + \frac{1}{1+l}\omega_i[4\psi - 2D(\psi) + 3\boldsymbol{e}_i \cdot \boldsymbol{e}_i(D(\psi) - \psi)](\boldsymbol{x}_b, t) \end{aligned} \tag{4.39}$$

parameterized with $l \geq 0$.

The second-order accuracy of the single-node scheme (4.39) can be simply explained as follows. First, two interpolations (4.34) and (4.36) are second-order accurate. In addition, for the diffusive scaling $\delta_t = \eta h^2$ (η is an adjustable parameter), the error of the approximation (4.38) is $O(h^2)$. Moreover, as shown in the previous section, the half-way anti-bounce-back scheme (4.35) has second-order accuracy. Therefore, the scheme (4.39) is second-order accurate.

Moreover, to ensure the stability of interpolations (4.34) and (4.36), it is required that the interpolation coefficients belong to $[0, 1]$, *i.e.*,

$$l \geq 0, \quad 1 - 2\gamma + l \geq 0 \quad \text{and} \quad 2\gamma - l \geq 0.$$

Table 1
Time steps for different s_ν and h in Example 5.1.

	$h = 1/40$	$h = 1/60$	$h = 1/80$	$h = 1/100$	$h = 1/120$
$s_\nu = 0.5$	1/320	1/720	1/1280	1/2000	1/2880
$s_\nu = 1$	1/960	1/2160	1/3840	1/6000	1/8640
$s_\nu = 1.5$	1/2880	1/6480	1/11520	1/18000	1/25920

Namely,

$$\max\{0, 2\gamma - 1\} \le l \le 2\gamma. \tag{4.40}$$

Remark 4.1. The above construction of the single-node scheme (4.39) is a direct application of that in [45]. The only difference is that here we use the anti-bounce-back scheme (3.29) as a central step while that in [45] is based on the bounce-back scheme for the no-slip boundary condition of the incompressible Navier-Stokes equations. As a consequence, the single-node schemes in [45] are all convex combinations of distributions functions, while the present scheme (4.39) is not a convex combination due to the minus in the first term of the anti-bounce-back scheme (3.29).

5. Numerical experiments

In this section, we conduct several numerical experiments to validate our model and boundary schemes. For the MRT model (2.2), there are infinitely many choice of relaxation rates. In the simulations, we only change the relaxation rate $s_\nu := s_3 = s_5$ related to the diffusion coefficient ν and fix all the others to examine the accuracy and stability. Without loss of generality, we take

$$\mathsf{S} = \mathrm{diag}(1, 1, 1, s_\nu, 1, s_\nu, 1, 1, 1). \tag{5.41}$$

Similar choice of S is also adopted in [23,36], where good computational results are obtained. Additionally, we show in the first example that the MRT model with the above S is superior over the BGK model ($s_i = s_\nu, i = 0, 1, \ldots, 8$) in terms of stability and accuracy.

For each experiment, we only need to specify the relaxation rate s_ν and the lattice size h, which determine all the other parameters: $\delta_t = \eta h^2$, $\eta = (\frac{1}{s_\nu} - \frac{1}{2})/(3\nu)$ and $c = 1/(\eta h)$. On the other hand, we only consider constant ν for simplicity. In order to verify the accuracy of the model and boundary schemes, we define the L^2-error as

$$E_r = \frac{\sqrt{\sum_{\boldsymbol{x}} |\phi(\boldsymbol{x}, T) - \phi^*(\boldsymbol{x}, T)|^2}}{\sqrt{\sum_{\boldsymbol{x}} |\phi(\boldsymbol{x}, T)|^2}}, \tag{5.42}$$

where the summation is taken over all the lattice nodes in the computational domain, ϕ^* is the LB solution, ϕ is the analytical solution and $T = 0.5$ is the terminal time.

Example 5.1. The first example is used to validate the LB model (2.2) and its advantages over the BGK model in terms of stability and accuracy. To do this, we construct a periodic problem with analytical solution

$$\phi(\boldsymbol{x}, t) = (t + 1)\sin(2\pi x)\cos(2\pi y), \qquad (x, y) \in [0, 1] \times [0, 1]. \tag{5.43}$$

The variables in (2.1) are taken as $\nu = 0.1$, $\boldsymbol{B} = (\phi, \phi)$ and $D(\phi) = \sin(\phi)$. Then the source term is

$$\begin{aligned} F &= \frac{\partial \phi}{\partial t} + \nabla \cdot \boldsymbol{B}(\phi) - \nabla \cdot [\nu \nabla D(\phi)] \\ &= \sin(2\pi x)cos(2\pi y) + 2\pi (t + 1)cos(2\pi x + 2\pi y) \\ &\quad + 0.4\pi^2 (t + 1)^2 \sin\big[(t + 1)\sin(2\pi x)\cos(2\pi y)\big]\cos^2(2\pi x)\cos^2(2\pi y) \\ &\quad + 0.4\pi^2 (t + 1)^2 \sin\big[(t + 1)\sin(2\pi x)\cos(2\pi y)\big]\sin^2(2\pi x)\sin^2(2\pi y) \\ &\quad + 0.8\pi^2 (t + 1)\cos\big[(t + 1)\sin(2\pi x)\cos(2\pi y)\big]\sin(2\pi x)\cos(2\pi y). \end{aligned} \tag{5.44}$$

The initial data is taken by setting $t = 0$ in (5.43).

In the computation, we take different $s_\nu (= 0.5, 1, 1.5)$ and $h = 1/40$, $1/60$, $1/80$, $1/100$, $1/120$. The corresponding time steps are provided in Table 1. The computational results are in good agreement with the analytical solution. For simplicity, we only show in Fig. 2 the result for $h = 1/100$ and $s_\nu = 1$. The convergence behaviors are plotted in Fig. 3. It can be seen that our model has second-order accuracy for different s_ν.

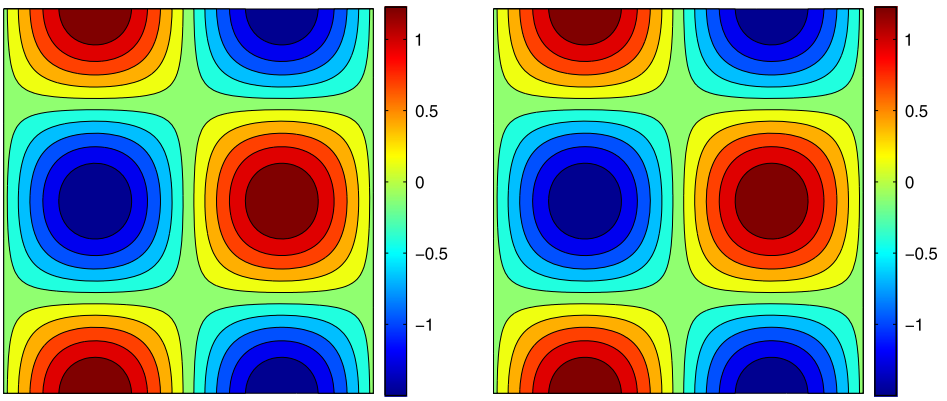

Fig. 2. Contour lines of ϕ for Example 5.1 at $T = 0.5$. Left: LB solution with $h = 1/100$ and $s_\nu = 1$, right: analytical solution.

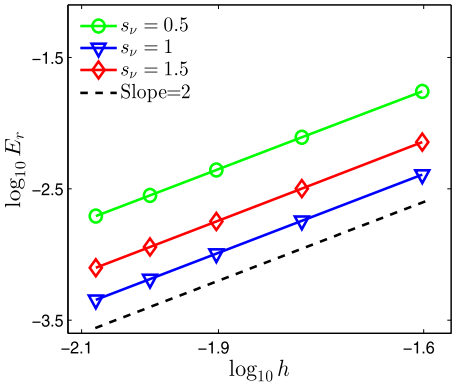

Fig. 3. Convergence order of the LB model for periodic problems in Example 5.1.

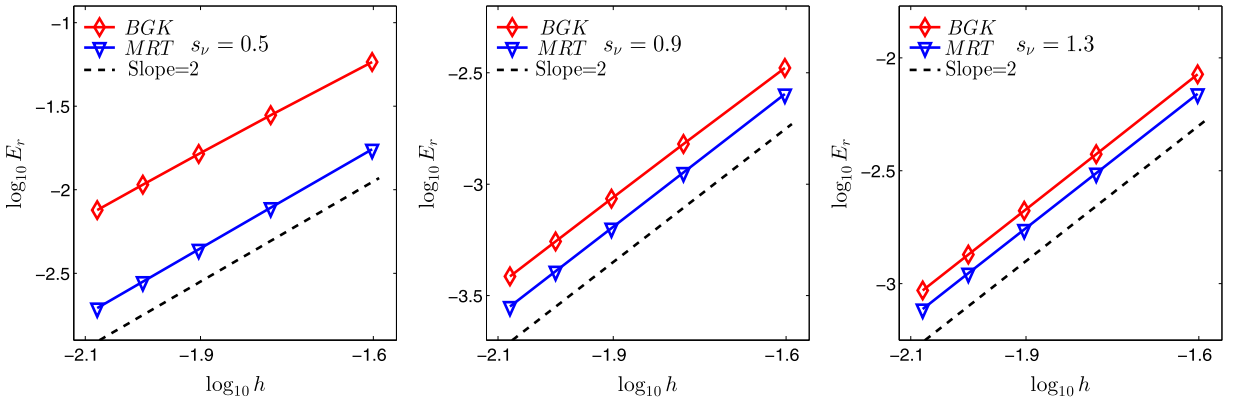

Fig. 4. Convergence orders of the BGK and MRT models for periodic problems in Example 5.1.

Next we use this example to compare the MRT (S is taken as (5.41)) and BGK ($s_i = s_\nu, i = 0, 1, \ldots, 8$) models in terms of stability and accuracy. To evaluate the stability, we fix $h = 1/120$ and search for an interval of s_ν in which the LB solution is convergent. Here by convergence we mean that the relative error defined in (5.42) is less than 10^{-2}. To avoid too large δ_t (for small s_ν), we only test $s_\nu \geq 0.4$. With a large number of numerical experiments, we obtain the stability intervals [0.4, 1.38] and [0.4, 1.71] for the BGK and MRT models, respectively. This indicates the superior stability of the MRT model. Furthermore, we take different $s_\nu (= 0.5, 0.9, 1.3)$ in both stability intervals and $h = 1/40, 1/60, 1/80, 1/100, 1/120$ to compare the errors. The convergence behaviors are plotted in Fig. 4. It can be seen that the convergence orders for both models are around 2, but the errors of the BGK model are larger those of the MRT model. The specific values of the errors are given in Table 2. These results demonstrate the better stability and accuracy of the MRT model over the BGK model. In addition, they support that the relaxation matrix in (5.41) is a good choice for the MRT model. But for the other choices, the superiority of the MRT model may not be guaranteed.

Table 2
L^2-error of the BGK and MRT models for periodic problems in Example 5.1.

h	$s_\nu = 0.5$		$s_\nu = 0.9$		$s_\nu = 1.3$	
	BGK	MRT	BGK	MRT	BGK	MRT
1/40	5.82×10^{-2}	1.75×10^{-2}	3.32×10^{-3}	2.54×10^{-3}	8.46×10^{-3}	6.93×10^{-3}
1/60	2.80×10^{-2}	7.81×10^{-3}	1.51×10^{-3}	1.13×10^{-3}	3.74×10^{-3}	3.09×10^{-3}
1/80	1.64×10^{-2}	4.40×10^{-3}	8.60×10^{-4}	6.35×10^{-4}	2.10×10^{-3}	1.74×10^{-3}
1/100	1.07×10^{-2}	2.82×10^{-3}	5.53×10^{-4}	4.06×10^{-4}	1.35×10^{-3}	1.11×10^{-3}
1/120	7.55×10^{-3}	1.96×10^{-3}	3.85×10^{-4}	2.82×10^{-4}	9.34×10^{-4}	7.72×10^{-4}

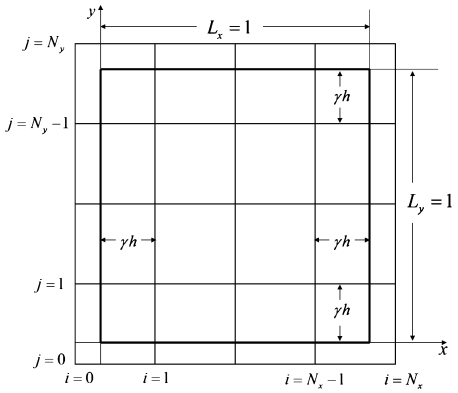

Fig. 5. Configuration of the mesh and straight boundaries. The thick straight lines are the boundaries of the computational domain. The thin lines are the grid lines. We take the same γ for different boundaries.

Table 3
Time steps for different s_ν and h in Example 5.2 with $\gamma = 0.5$.

	$h = 1/20$	$h = 1/40$	$h = 1/60$	$h = 1/80$	$h = 1/100$
$s_\nu = 0.5$	1/800	1/3200	1/7200	1/12800	1/2000
$s_\nu = 1$	1/2400	1/9600	1/21600	1/38400	1/60000
$s_\nu = 1.5$	1/7200	1/28800	1/64800	1/115200	1/180000
$s_\nu = 1.9$	1/15200	1/60800	1/136800	1/243200	1/380000

Example 5.2. In the second example, we verify the accuracy of the anti-bounce-back scheme (3.29) with the solution

$$\phi(\boldsymbol{x}, t) = t\cos[2\pi xy(1-xy)]$$

in a square domain $\Omega = \{(x, y) \mid 0 \le x, y \le 1\}$. Then the boundary condition is

$$\phi(\boldsymbol{x}_b, t) = t\cos[2\pi x_b y_b(1 - x_b y_b)], \quad \boldsymbol{x}_b := (x_b, y_b) \in \partial\Omega$$

and the initial data is also determined by the above solution. We take $\nu = 1$, $\boldsymbol{B} = (\phi, \phi)$, $D := D(\phi) = \phi^2 + \phi$ and F is similarly obtained as (5.44). The anti-bounce-back scheme (3.29) is applied at all the straight boundaries.

The mesh for the computation is illustrated in Fig. 5. In the figure, N_x and $N_y (= N_x)$ are the number of meshes in the horizontal and vertical directions, respectively. We take the same γ for different boundaries. Then the lattice size is

$$h = \frac{1}{N_x - 2 + 2\gamma}. \tag{5.45}$$

To demonstrate the accuracy and stability of the scheme, we set $\gamma = 0.2$, 0.5 and 0.8, and take different $s_\nu (= 0.5, 1, 1.5, 1.9)$ and $N_x (= 21, 41, 61, 81, 101)$. The time steps for $\gamma = 0.5$ are listed in Table 3. Fig. 6 shows that convergence orders are all around 2 for the half-way anti-bounce-back scheme ($\gamma = 0.5$) with different s_ν. However, when $\gamma = 0.2$ and 0.8, the convergence orders are only 1. These results confirm our analysis in Section 3. Additionally, we see from Fig. 6 that the errors are not sensitive to the value of s_ν.

Example 5.3. With the same problem and mesh in Example 5.2, we further demonstrate the single-node scheme (4.39) for straight boundaries. The scheme is used at all the boundaries in Fig. 5. In the computation, we take $l = \gamma, 1.5\gamma, \gamma^2$ and $\gamma^2 + \gamma$, which all satisfy (4.40). The convergence behaviors are shown in Fig. 7. It is clear that the convergence orders are

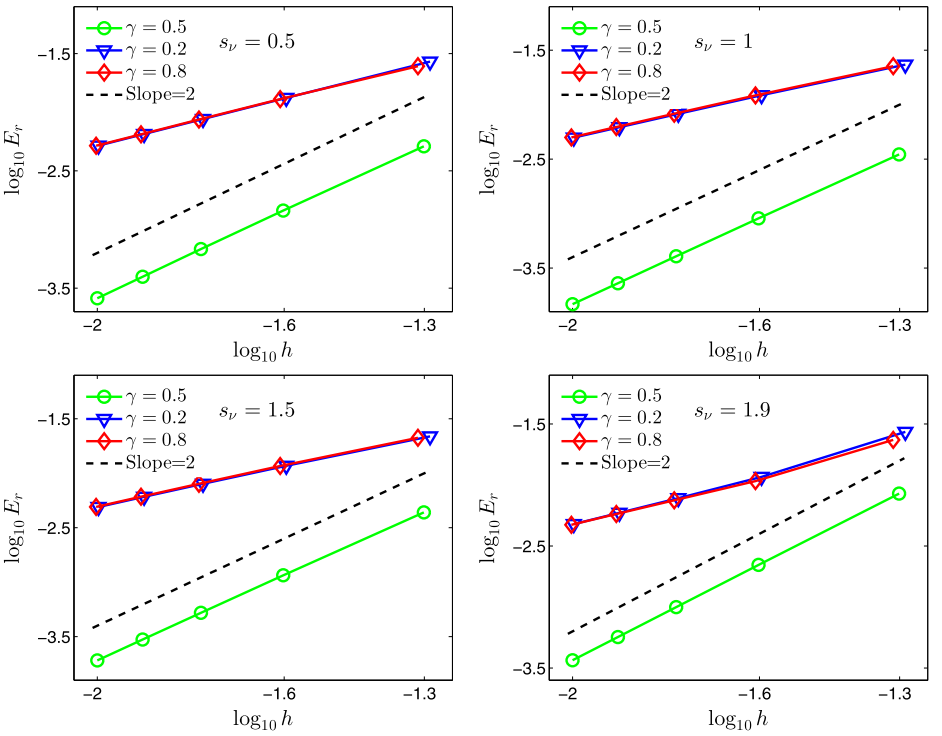

Fig. 6. Convergence order of the anti-bounce-back scheme with different γ for the straight boundary.

all around 2 for different γ, l and s_ν. These show the second-order accuracy and good stability of the single-node scheme (4.39) for straight boundaries.

Example 5.4. In this example, we consider a circular domain

$$\Omega := \left\{ (x, y) \mid (x - \frac{1}{2})^2 + (y - \frac{1}{2})^2 \leq \frac{1}{16} \right\}$$

to demonstrate the single-node scheme (4.39) for curved boundaries. To this end, we construct the following solution

$$\phi = (t + 1) \sin[2\pi xy(1 - x)(1 - y)] \tag{5.46}$$

in the circular domain defined above. The initial data and boundary values are determined by the solution (5.46). Similarly, we set $\nu = 1$, $\boldsymbol{B} = (\phi, \phi)$, $D := D(\phi) = \phi^2 + \phi$ and F is obtained as (5.44). We take different $s_\nu (= 0.5, 1, 1.5, 1.9)$ and $h (= 1/40, 1/80, 1/120, 1/160, 1/200)$ to examine the stability and accuracy. As an example, we show in Fig. 8 the comparison between the analytical solution and the LB solution with $l = \gamma^2$, $h = 1/120$ and $s_\nu = 1.5$. From the figure we see that good agreements are obtained by the single-node scheme. Fig. 9 shows that even with the curved boundary, the sing-node scheme has second-order accuracy for different s_ν. Thus the single-node scheme (4.39) is applicable to curved boundaries.

6. Conclusions and remarks

In this work, we are concerned with the LBM for general nonlinear CDEs. We develop a MRT LB model for the general equations by using the equilibrium distribution function in [19] without the integration term. We show that the macroscopic equations can be correctly recovered under the diffusive scaling. The accuracy of the anti-bounce-back scheme accompanying the MRT model is analyzed with the Maxwell iteration. We clearly justify, based on an elegant relation for the collision matrix found in [45], that the scheme is second-order accurate when the boundary is located at the middle of two lattice nodes. To the best of our knowledge, this is the first time that the second-order accuracy of the half-way anti-bounce-back scheme is rigorously analyzed for the MRT model. Furthermore, by using the half-way anti-bounce-back scheme as a central step, we construct some parameterized single-node second-order schemes for curved boundaries with the approach in [45]. Finally, numerical experiments are conducted to validate the accuracy of the proposed model and boundary schemes. In addition, the superiority of the MRT model over the BGK model is also numerically demonstrated in terms of stability and accuracy.

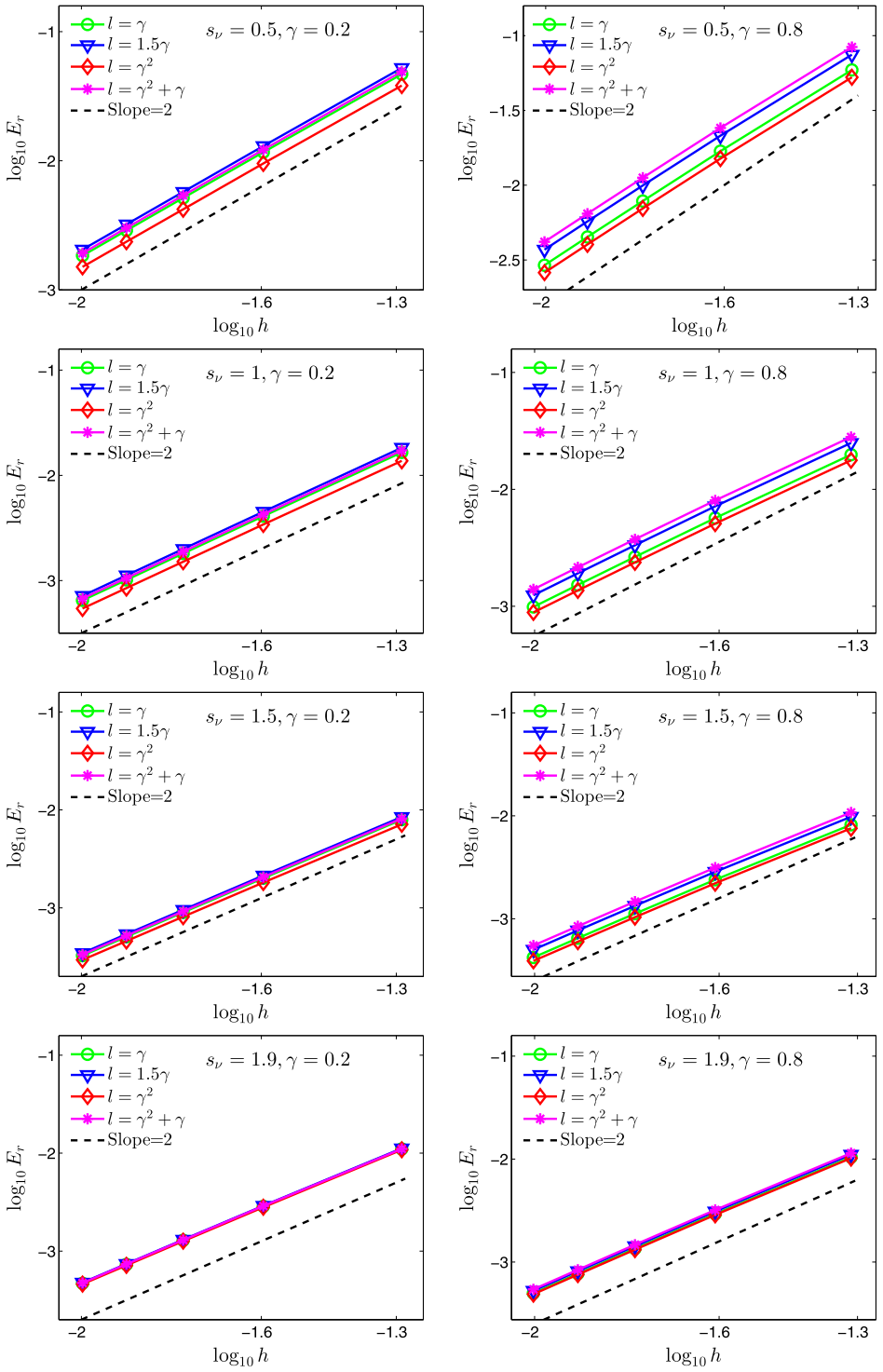

Fig. 7. Convergence order of the single-node boundary scheme for the straight boundary. Left: $\gamma = 0.2$, right: $\gamma = 0.8$. From top to bottom: $s_\nu = 0.5$, 1, 1.5 and 1.9.

We would like to point out that, owing to the diffusive scaling, the consistency of the present model needs neither assumptions on the smallness of derivatives of the convection or diffusion terms in [24], nor the integration and time derivatives in [19]. In fact, using the diffusive scaling is quite common for explicit difference schemes of CDEs because of the diffusion terms [6,7]. Thus it is also natural for the LBM, which indeed is a special explicit finite difference scheme.

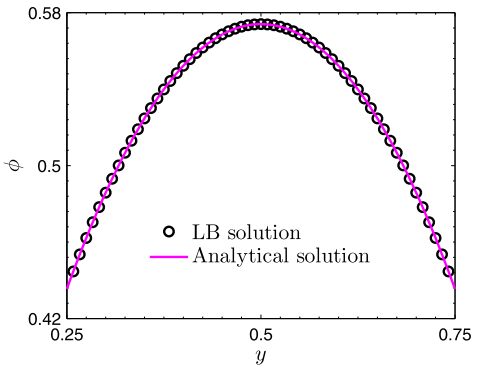

Fig. 8. Comparison of the LB solution and the analytical solution along the vertical center line $x = 0.5$ in Example 5.4.

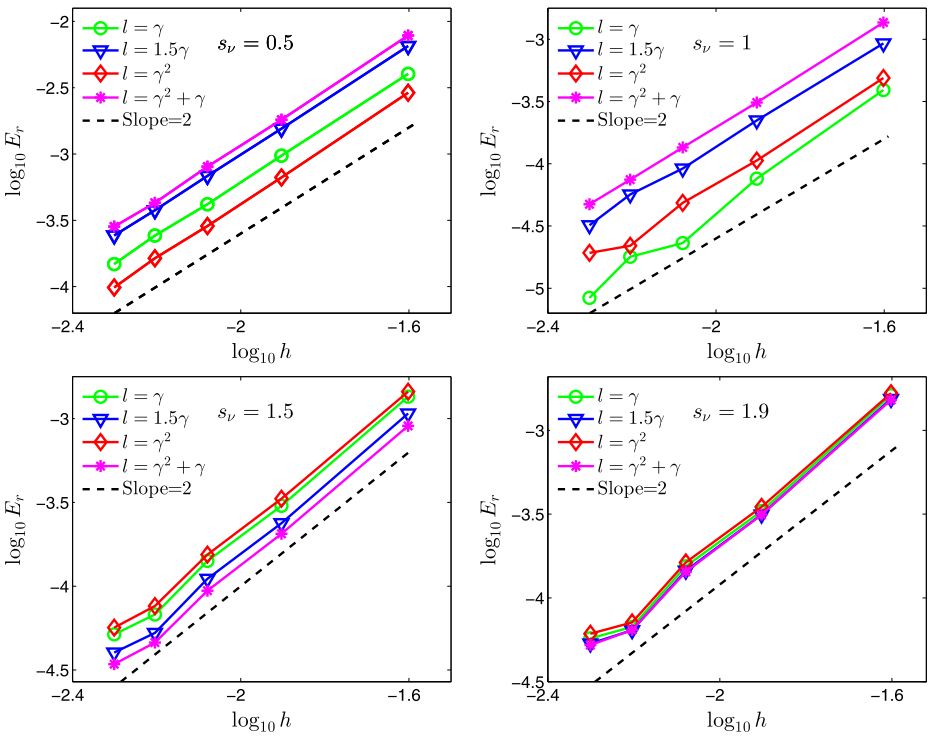

Fig. 9. Convergence order of the single-node schemes for curved boundaries with different s_ν.

On the other hand, the present MRT model degenerates to the classical model when the macroscopic equations are linear (see *e.g.*, [29,46]). For the latter, the convergence is established in [46] based on the stability structure proposed in [47,48]. This structure may also be crucial for the convergence analysis of the present model, but how it can be used here remains open problems due to the nonlinearity. We will study this interesting topic in the next step.

Finally, though the present model is proposed for isotropic CDEs, it can be easily extended to anisotropic case with the ideas in [30,23]. Additionally, it is also possible to develop third-order models and boundary schemes for general CDEs [25, 49,50], which will be left for the future.

Acknowledgements

We would like to thank the referee for the valuable comments and suggestions, which helped us to improve the paper. W. Zhao was supported by the China Postdoctoral Science Foundation (2017M620603), the Fundamental Research Funds for the Central Universities (FRF-TP-17-068A1), and the National Natural Science Foundation of China (No. 11801030). P. Lin was supported by the National Natural Science Foundation of China (No. 91430106, No. 11771040).

Appendix

This appendix is devoted to the derivation of (2.14). To begin with, we use (3.23) to compute

$$\begin{aligned}[\tilde{D}^{(3)}\mathbf{m}^{(eq)}]_0 &= \frac{1}{6}[(\tilde{D}^{(1)})^3\mathbf{m}^{(eq)}]_0 + \eta\partial_t[\tilde{D}^{(1)}\mathbf{m}^{(eq)}]_0 \\ &= \frac{1}{6}[(\tilde{D}^{(1)})^3\mathbf{m}^{(eq)}]_0 + O(h) \\ &= \frac{1}{6}\sum_i(\boldsymbol{e}_i\cdot\nabla)^3 f_i^{(eq)} + O(h) = O(h).\end{aligned}$$

Here for the last equality we have used the property that $(\boldsymbol{e}_i\cdot\nabla)^3$ is odd. Thus (2.14a) holds. For (2.14b), it is easy to see from (2.12) that

$$[\mathsf{S}^{-1}\tilde{D}^{(1)}\mathbf{m}^{(eq)}]_{0,1,7,8} = O(h). \tag{6.47}$$

With this and the explicit expressions of $\tilde{\mathsf{E}}_x$ and $\tilde{\mathsf{E}}_y$, we have

$$\{[\mathsf{S}^{-1}\tilde{D}^{(1)}]^2\mathbf{m}^{(eq)}\}_{3,5} = O(h)$$

and

$$\{[\mathsf{S}^{-1}\tilde{D}^{(1)}]^3\mathbf{m}^{(eq)}\}_0 = O(h).$$

The above equation is exactly (2.14b). Moreover, using

$$\begin{aligned}&\tilde{D}^{(1)}\mathsf{S}^{-1}\tilde{D}^{(2)} = \frac{1}{2}\tilde{D}^{(1)}\mathsf{S}^{-1}(\tilde{D}^{(1)})^2 + \eta\partial_t\tilde{D}^{(1)}\mathsf{S}^{-1}, \\ &[\tilde{D}^{(1)}\mathsf{S}^{-1}\mathbf{m}^{(eq)}]_0 = O(h),\end{aligned}$$

and (6.47), we have

$$[\mathsf{S}^{-1}(\tilde{D}^{(1)})^2\mathbf{m}^{(eq)}]_{3,5} = O(h)$$

and

$$[\tilde{D}^{(1)}\mathsf{S}^{-1}(\tilde{D}^{(1)})^2\mathbf{m}^{(eq)}]_0 = O(h).$$

Then (2.14c) holds. Similarly, (2.14d) can be derived easily. Thus we have shown (2.14).

References

[1] Y. Wang, L.Y. Li, C.L. Page, A two-dimensional model of electrochemical chloride removal from concrete, Comput. Mater. Sci. 20 (2) (2001) 196–212.
[2] T. Inamuro, T. Ogata, S. Tajima, N. Konishi, A lattice Boltzmann method for incompressible two-phase flows with large density differences, J. Comput. Phys. 198 (2) (2004) 628–644.
[3] J.P. Butler, The Green's function for the convection-diffusion equation in an analytic lung model, Bull. Math. Biol. 39 (5) (1977) 543–563.
[4] L.C. Evans, Partial Differential Equations, 2nd ed., American Mathematical Society, 2010.
[5] B.H. Gilding, R. Kersner, Travelling Waves in Nonlinear Diffusion-Convection Reaction, Progress in Nonlinear Differential Equations and Their Applications, vol. 60, Springer Basel AG, 2004.
[6] K.W. Morton, Numerical Solution of Convection-Diffusion Problems, Chapman and Hall, 1996.
[7] K.W. Morton, D.F. Mayers, Numerical Solution of Partial Differential Equations, 2nd ed., Cambridge University Press, 2005.
[8] B.R. Baliga, S.V. Patankar, A new finite-element formulation for convection-diffusion problems, Numer. Heat Transf. 3 (4) (1980) 393–409.
[9] E. Herbert, S. Joachim, A hybrid mixed discontinuous Galerkin finite-element method for convection-diffusion problems, IMA J. Numer. Anal. 30 (4) (2018) 1206–1234.
[10] G. Manzini, A. Russo, A finite volume method for advection-diffusion problems in convection-dominated regimes, Comput. Methods Appl. Mech. Eng. 197 (13) (2008) 1242–1261.
[11] S. Phongthanapanich, P. Dechaumphai, Finite volume method for convection-diffusion-reaction equation on triangular meshes, Int. J. Numer. Methods Biomed. Eng. 26 (6) (2010) 716–727.
[12] Z.F. Tian, S.Q. Dai, High-order exponential finite difference methods for convection-diffusion type problems, J. Comput. Phys. 220 (2) (2007) 952–974.
[13] X. Xiang, Z. Wang, B. Shi, Modified lattice Boltzmann scheme for nonlinear convection diffusion equations, Commun. Nonlinear Sci. Numer. Simul. 17 (2012) 2415–2425.
[14] Y. Hu, D. Li, S. Shu, X. Niu, Lattice Boltzmann flux scheme for the convection–diffusion equation and its applications, Comput. Math. Appl. 72 (2016) 48–63.
[15] S. Succi, The Lattice Boltzmann Equation for Fluid Dynamics and Beyond, Oxford University Press, Oxford, 2001.
[16] Z. Guo, C. Shu, Lattice Boltzmann Method and Its Applications in Engineering, Word Scientific Publishing Company, Singapore, 2013.
[17] S.P. Dawson, S. Chen, G.D. Doolen, Lattice Boltzmann computations for reaction-diffusion equations, J. Chem. Phys. 98 (2) (1993) 1514–1523.
[18] B. Chopard, J.L. Falcone, J. Latt, The lattice Boltzmann advection-diffusion model revisited, Eur. Phys. J. Spec. Top. 171 (1) (2009) 245–249.
[19] B. Shi, Z. Guo, Lattice Boltzmann model for nonlinear convection-diffusion equations, Phys. Rev. E 79 (2009) 016701.

[20] Z. Chai, T.S. Zhao, Lattice Boltzmann model for the convection-diffusion equation, Phys. Rev. E 87 (2013) 063309.
[21] Q. Li, Z. Chai, B. Shi, Lattice Boltzmann model for a class of convection-diffusion equations with variable coefficients, Comput. Math. Appl. 70 (4) (2015) 548–561.
[22] L. Wang, B. Shi, Z. Chai, Regularized lattice Boltzmann model for a class of convection-diffusion equations, Phys. Rev. E 92 (2015) 043311.
[23] Z. Chai, B. Shi, Z. Guo, A multiple-relaxation-time lattice Boltzmann model for general nonlinear anisotropic convection-diffusion equations, J. Sci. Comput. 69 (1) (2016) 1–36.
[24] I. Ginzburg, Equilibrium-type and link-type lattice Boltzmann models for generic advection and anisotropic-dispersion equation, Adv. Water Resour. 28 (11) (2005) 1171–1195.
[25] I. Ginzburg, Generic boundary conditions for lattice Boltzmann models and their application to advection and anisotropic dispersion equations, Adv. Water Resour. 28 (11) (2005) 1196–1216.
[26] I. Ginzburg, Lattice Boltzmann modeling with discontinuous collision components: hydrodynamic and advection-diffusion equations, J. Stat. Phys. 126 (1) (2006) 157–206.
[27] I. Ginzburg, Truncation errors, exact and heuristic stability analysis of two-relaxation-times lattice Boltzmann schemes for anisotropic advection-diffusion equation, Commun. Comput. Phys. 11 (5) (2012) 1439–1502.
[28] I. Ginzburg, Multiple anisotropic collisions for advection-diffusion lattice Boltzmann schemes, Adv. Water Resour. 51 (1) (2013) 381–404.
[29] J. Huang, W.-A. Yong, Boundary conditions of the lattice Boltzmann method for convection-diffusion equations, J. Comput. Phys. 300 (2015) 70–91.
[30] R. Huang, H. Wu, A modified multiple-relaxation-time lattice Boltzmann model for convection-diffusion equation, J. Comput. Phys. 274 (2014) 50–63.
[31] I. Rasin, S. Succi, W. Miller, A multi-relaxation lattice kinetic method for passive scalar diffusion, J. Comput. Phys. 206 (2005) 453–462.
[32] H. Yoshida, M. Nagaoka, Multiple-relaxation-time lattice Boltzmann model for the convection and anisotropic diffusion equation, J. Comput. Phys. 229 (2010) 7774–7795.
[33] H. Yoshida, M. Nagaoka, Lattice Boltzmann method for the convection–diffusion equation in curvilinear coordinate systems, J. Comput. Phys. 257 (2014) 884–900.
[34] L. Li, C. Chen, R. Mei, J.F. Klausner, Conjugate heat and mass transfer in the lattice Boltzmann equation method, Phys. Rev. E 89 (2014) 043308.
[35] L. Li, R. Mei, J.F. Klausner, Lattice Boltzmann models for the convection-diffusion equation: D2Q5 vs D2Q9, Int. J. Heat Mass Transf. 108 (2017) 41–62.
[36] Z. Chai, T.S. Zhao, Nonequilibrium scheme for computing the flux of the convection-diffusion equation in the framework of the lattice Boltzmann method, Phys. Rev. E 90 (2014) 013305.
[37] Z. Guo, C. Zheng, B. Shi, An extrapolation method for boundary conditions in lattice Boltzmann method, Phys. Fluids 14 (6) (2002) 2007–2010.
[38] M. Junk, Z. Yang, One-point boundary condition for the lattice Boltzmann method, Phys. Rev. E 72 (2005) 066701.
[39] A. Eshghinejadfard, D. Thévenin, Numerical simulation of heat transfer in particulate flows using a thermal immersed boundary lattice Boltzmann method, Int. J. Heat Fluid Flow 60 (2016) 31–46.
[40] Z. Yu, X. Shao, A. Wachs, A fictitious domain method for particulate flows with heat transfer, J. Comput. Phys. 2172 (2006) 424–452.
[41] D. d'Humières, in: B.D. Shizgal, D.P. Weave (Eds.), Rarefied Gas Dynamics: Theory and Simulations, AIAA, Washington, D.C., 1992, in: Prog. Astronaut. Aeronaut., vol. 159, 1992, p. 450.
[42] P. Lallemand, L.-S. Luo, Theory of the lattice Boltzmann method: dispersion, dissipation, isotropy, galilean invariance, and stability, Phys. Rev. E 61 (2000) 6546–6562.
[43] W.-A. Yong, W. Zhao, L.-S. Luo, Theory of the lattice Boltzmann method: derivation of macroscopic equations via the Maxwell iteration, Phys. Rev. E 93 (2016) 033310.
[44] W. Zhao, W.-A. Yong, Maxwell iteration for the lattice Boltzmann method with diffusive scaling, Phys. Rev. E 95 (2017) 033311.
[45] W. Zhao, J. Huang, W.-A. Yong, Boundary conditions for kinetic theory based models I: lattice Boltzmann models, submitted for publication.
[46] M. Junk, Z. Yang, L_2 convergence of the lattice Boltzmann method for one dimensional convection-diffusion-reaction equations, Commun. Comput. Phys. 17 (5) (2015) 1225–1245.
[47] M.K. Banda, W.-A. Yong, A. Klar, A stability notion for lattice Boltzmann equations, SIAM J. Sci. Comput. 27 (6) (2006) 2098–2111.
[48] M. Junk, W.-A. Yong, Weighted L^2-stability of the lattice Boltzmann method, SIAM J. Numer. Anal. 47 (3) (2009) 1651–1665.
[49] F. Dubois, P. Lallemand, Towards higher order lattice Boltzmann schemes, J. Stat. Mech. Theory Exp. 2009 (6) (2009) 06006.
[50] F. Dubois, P. Lallemand, M. Tekitek, On a superconvergent lattice Boltzmann boundary scheme, Comput. Math. Appl. 59 (7) (2010) 2141–2149.